

# Spectral and Transport Properties of Quark-Gluon Plasma in a Nonperturbative Approach

Shuai Y.F. Liu<sup>1</sup> and Ralf Rapp<sup>1</sup>

Department of Physics and Astronomy and Cyclotron Institute, Texas A&M University, College Station, TX 77843-3366, USA

Received: March 30, 2020/ Revised version:

**Abstract.** Nonperturbative methods play an important role in quantum many-body systems, especially in situations with an interplay of continuum and bound states and/or large coupling strengths between the constituents. Employing the Luttinger-Ward functional (LWF) we have computed the equation of state (EoS) of the quark-gluon plasma (QGP) using fully dressed selfconsistent 1- and 2-body propagators. We first give an alternative derivation of our previously reported results for resumming the ladder diagram series of the LWF using a “matrix log” technique which accounts for dynamically formed bound and resonant states. Two types of solutions were found in selfconsistent fits to lattice-QCD data for the EoS, heavy-quark free energy and quarkonium correlators: a strongly coupled scenario (SCS) with broad parton spectral functions and strong meson resonances near the transition temperature vs. a weakly coupled scenario (WCS) with well-defined parton quasiparticles and weak meson resonances. Here, we discuss how these solutions can be distinguished by analyzing the pertinent transport properties. We focus on the specific shear viscosity,  $(4\pi)\eta/s$ , and the heavy-quark diffusion coefficient,  $(2\pi T)\mathcal{D}_s$ , including its mass dependence. At low temperatures, in the SCS, they turn out to be a factor of 2 within their conjectured quantum lower bound, while they are a factor of 2-5 larger in the WCS. At higher temperatures, the transport parameters of the two scenarios approach each other. We propose the ratio  $(4\pi\eta/s)/(2\pi T\mathcal{D}_s)$  as a measure to distinguish the perturbative and strong-coupling limits of 5/2 and 1, respectively.

**PACS.** 12.38.Mh Quark-gluon plasma – 52.27.Gr Strongly-coupled plasmas – 51.30.+i Thermodynamic properties, equations of state

## 1 Introduction

The theoretical investigation of the quark-gluon plasma (QGP) remains a challenging task in nuclear research. Of particular interest are its spectral and transport properties, which can be related to observables in ultrarelativistic heavy-ion collisions (URHICs). These quantities are not easily extracted from first-principles lattice-QCD (lQCD) computations [1] which are performed in euclidean space-time. Various other theoretical tools, including Dyson-Schwinger, functional-renormalization group and Polyakov-Nambu-Jona-Lasinio approaches [2,3,4,5,6,7], are being pursued to meet this challenge. In the present work, we employ a thermodynamic  $T$ -matrix approach, which was originally designed to describe heavy quarks and quarkonia in the QGP [8,9]. More recently, it has been extended to the light sector to connect the in-medium properties of heavy quarks to those of the QGP bulk medium [10]. The  $T$ -matrix approach utilizes a ladder resummation where the interaction kernel is based on a potential approximation while keeping the full dynamical information in the one- and two-body spectral functions. This enables to directly calculate in real time and account for long-range nonperturbative interactions, thus facilitating in-

sights into QGP properties that are complementary to other approaches as mentioned above. Among its benefits is the capability to evaluate various quantities, encompassing transport, spectral and bulk properties, within a rigorous many-body framework on the same footing. In this way one can investigate interrelations between the microscopic structure of the QGP and its macroscopic properties as inferred from URHIC phenomenology [11,12,13,14,15].

Within the  $T$ -matrix approach we employ a QCD-inspired Hamiltonian, where, in the spirit of an effective field theory, the inputs in form of an in-medium potential and bare masses (“Wilson coefficients”) are matched to QCD utilizing lattice “data” for quarkonium correlation functions, the HQ free energy, as well as the QGP equation of state (EoS). This is carried out in a self-consistent Luttinger-Ward-Baym (LWB) formalism [16,17,18] for the EoS, which accounts for the full off-shell dynamics of the in-medium particle propagators and scattering amplitudes in a conserving approximation. In particular, the bound-state contribution to the EoS, encoded in the Luttinger-Ward functional (LWF),  $\Phi$ , is incorporated through a full resummation of the  $t$ -channel ladder diagrams utilizing a numerical matrix-logarithm

method. While we have employed this method before in a 3-dimensional (3D) reduced version [19, 10], the present paper contains an alternative derivation in a full 4D context, although the practical application will still be carried out in a 3D-reduced form. The main new application in the present paper is the calculation of transport coefficients, specifically the shear viscosity of the bulk medium and the spatial HQ diffusion constant including a study of its HQ mass dependence. These will provide new insights into how they relate to each other and to the underlying spectral properties of partons and their 2-body correlations.

Our paper is organized as follows. In Sec. 2, we briefly discuss the main components of the many-body formalism, containing the 4D derivation for the resummation of the LWF. In Sec. 3, we recall the inputs corresponding to 2 limiting scenarios (strongly coupled scenario (SCS) and weakly coupled scenario (WCS)) as identified in our previous work, and summarize the key features of the pertinent spectral properties in Sec. 4. In Sec. 5, we calculate the transport coefficients for both coupling scenarios and propose their ratio as a novel measure to assess the coupling strength of the medium. In Sec. 6, we summarize our main results and conclude.

## 2 Many-Body Formalism

In this section, we lay out the many-body formalism in a self-contained form. In particular, the nonperturbative evaluation of the EoS is derived in a 4D version that goes beyond our previous work [10]. Although the practical application in the present paper will utilize a 3D reduced form, the framework can in principle be deployed to 4D approaches such as Dyson-Schwinger.

We start from the grand potential as a functional of the fully dressed single-particle propagator,  $G$ ,

$$\Omega(G) = \mp \text{Tr} \{ \ln(-G^{-1}) + (G_0^{-1} - G^{-1})G \} \pm \Phi(G), \quad (1)$$

where the trace (Tr) indicates 3-momentum ( $\mathbf{p}$ ) integrations and summations over Matsubara frequencies ( $\omega_n$ ) and internal degrees of freedom (*e.g.*, spin and flavor);  $G_0$  denotes the bare propagator. The single-particle self-energy can be expressed as a functional derivative of the LWF,

$$\Sigma(G) = \beta \delta \Phi(G) / \delta G, \quad (2)$$

where  $\Phi(G)$  is usually constructed by a skeleton expansion to finite loop order [20] ( $\beta = 1/T$  is the inverse temperature). Here we consider a situation where the selfenergy,  $\Sigma(G)$ , is calculated from a  $T$ -matrix amplitude with kernel  $V$ , with formal solutions

$$T = V + VGGT = (1 - VGG)^{-1}V \quad (3)$$

$$\Sigma(G) = TG = (1 - VGG)^{-1}VG. \quad (4)$$

Integrating Eq. (2), together with Eq. (4), yields

$$\begin{aligned} \Phi(G) &= \frac{1}{\beta} \int dG (1 - VGG)^{-1} VG = -\frac{1}{2\beta} \ln(1 - VGG) \\ &= \frac{1}{2\beta} \{ VG + \frac{1}{2} VGGVG + \dots + \frac{1}{\nu} VGG \dots VG \} G. \end{aligned} \quad (5)$$

The second line recovers the standard skeleton expansion,

$$\Phi(G) = \frac{1}{2} \text{Tr} \sum_{\nu=1}^{\infty} \frac{1}{\nu} \Sigma_{\nu}(G)G, \quad (6)$$

where  $\Sigma_{\nu}(G)$  represents the  $\nu^{\text{th}}$  order in the interaction in the skeleton diagram, expressed as a functional of  $G$  [16]. The formally integrated form in the first line of Eq. (5) is a nonperturbative expression which remains finite for large  $V$ , for which the perturbative series in the second line is usually divergent. This calls for a practical method to evaluate the functional integral in Eq. (5).

Toward this end we resolve this expression into discrete energy-momentum indices (similar to the discretization of the  $T$ -matrix integral equation [21]), and convert the log-function into a matrix representation. Considering 4-momentum as a single discretized variable, one can write the 2-body interaction kernel and single-particle propagators as

$$\begin{aligned} \mathbb{V}_{ij} &\equiv V(\tilde{k}_i, \tilde{k}_j) \\ \mathbb{G}_{ij} &\equiv G(\tilde{k}_i) \delta_{ij}, \quad \mathbb{G}(\tilde{P})_{ij} \equiv G(\tilde{P} - \tilde{k}_i) \delta_{ij}, \end{aligned} \quad (7)$$

where  $\tilde{k}_{i,j} = (i\omega_n, \mathbf{k})_{i,j}$  are relative in- and outgoing 4-momenta in Matsubara representation, and  $\tilde{P}$  is the total 2-particle 4-momentum in the heat bath. With this notation one recovers the standard inverse-matrix solution [21] to the  $T$ -matrix as

$$\mathbb{T}(\tilde{P}) = [(1 - \mathbb{V}\mathbb{G}\mathbb{G}(\tilde{P}))^{-1}] \mathbb{V}, \quad (8)$$

with  $T(\tilde{p}, \tilde{q} | \tilde{p}', \tilde{q}')$  written as  $T(\tilde{P} - \tilde{k}_i, \tilde{k}_i | \tilde{P} - \tilde{k}_j, \tilde{k}_j) = \mathbb{T}(\tilde{P})_{ij}$ . We can now evaluate the logarithm in Eq. (5) using a matrix representation, denoted by “Log”, as<sup>1</sup>

$$\Phi = -\frac{1}{2} \int d^4 \tilde{P} \text{Tr} \left\{ \text{Log} \left[ 1 - \mathbb{V}\mathbb{G}\mathbb{G}(\tilde{P}) \right] \right\}. \quad (9)$$

The “Tr” of the matrix includes relative 4-momentum and internal degrees of freedom, and is followed by a scalar integration over  $\tilde{P}$ . Equation (9) constitutes a practical formula to compute the ladder series of the LWF exactly; it is an example of a primitive functional of  $\Sigma(G)$ , *i.e.*, a category of functional integrals which can be carried out by a matrix function.

We perform the Log operation by recasting the LWF as

$$\Phi = \frac{1}{2} \int d^4 \tilde{p} \ln \Sigma(\tilde{p}) G(\tilde{p}). \quad (10)$$

<sup>1</sup> A similar expression is known for the ground-state energy at zero temperature [22] and for cold-atom systems [23].

This can be seen by augmenting the  $\mathbb{L}\text{og}$  in Eq. (9) with  $1=[\mathbb{G}\mathbb{G}(\tilde{P})]^{-1}[\mathbb{G}\mathbb{G}(\tilde{P})]$  and combining it with the first (inverse) factor to obtain

$$\mathbb{L}\text{og}\mathbb{T}(\tilde{P}) = -\mathbb{L}\text{og} \left[ \mathbb{1} - \mathbb{V}\mathbb{G}\mathbb{G}(\tilde{P}) \right] [\mathbb{G}\mathbb{G}(\tilde{P})]^{-1}. \quad (11)$$

With  $\mathbb{L}\text{og}\mathbb{T}(\tilde{P})_{ij} = \ln T(\tilde{P} - \tilde{k}_i, \tilde{k}_i | \tilde{P} - \tilde{k}_j, \tilde{k}_j)$ , we contract the diagonal forward-scattering  $T$ -matrix with  $G$ ,

$$\ln \Sigma(\tilde{p}) \equiv \int d^4 \tilde{q} \ln T(\tilde{p}, \tilde{q} | \tilde{p}, \tilde{q}) G(\tilde{q}), \quad (12)$$

which, together with the remaining propagator  $G$ , recovers Eq. (10); note the formal similarity of Eq. (10) with the skeleton expansion, Eq. (6). With this setup, the only change in going from the selfconsistent selfenergy,

$$\Sigma(\tilde{p}) = \int d^4 \tilde{q} T(\tilde{p}, \tilde{q} | \tilde{p}, \tilde{q}) G(\tilde{q}), \quad (13)$$

to the LWF is replacing the inverse-matrix solution for  $T$  from Eq. (8) by the matrix-logarithm,  $\ln T$ , from Eq. (11) (and the factor  $\mathbb{V}$  by  $\mathbb{G}\mathbb{G}^{-1}$ ). Standard techniques used to calculate the  $T$ -matrix, such as 3D reductions of the Bethe-Salpeter equation [24], partial-wave expansions and center-of-mass (CM) approximations [25,26], can be also be applied to calculate  $\ln T$ , cf. also Refs. [19,10].

We deploy this formalism to the QGP within a Hamiltonian approach, systematically benchmarked by constraints from IQCD [27,28,29,30,31]. Our main approximation is that the relevant interactions can be encoded in a potential-like driving kernel. Importantly, this allows to include remnants of the confining force above  $T_{pc}$ , for which there is ample evidence from IQCD [30,32]. The effective Hamiltonian is of the form

$$H = \sum \varepsilon(p) \psi^\dagger(\mathbf{p}) \psi(\mathbf{p}) + \frac{1}{2} \psi^\dagger\left(\frac{\mathbf{P}}{2} - \mathbf{p}\right) \psi^\dagger\left(\frac{\mathbf{P}}{2} + \mathbf{p}\right) V \psi\left(\frac{\mathbf{P}}{2} + \mathbf{p}'\right) \psi\left(\frac{\mathbf{P}}{2} - \mathbf{p}'\right), \quad (14)$$

where the summation is over momentum, spin, color and flavor ( $N_f=3$  anti-/quarks plus gluons; for simplicity we assume spin degeneracy), and  $\varepsilon(p)=\sqrt{M^2 + \mathbf{p}^2}$  with bare parton masses,  $M$ . The effective gluon is treated with a single-pole propagator in our approach. Thus, some expressions will differ by a factor of 1/2 compared to those using a fully relativistic gluon propagator. For the 2-body potential we make the ansatz

$$V(\mathbf{p}, \mathbf{p}') = \mathcal{F}^C V_C(\mathbf{q}) B(p, p') + \mathcal{F}^S V_S(\mathbf{q}) / R(p, p') \quad (15)$$

where  $\mathbf{q} = \mathbf{p} - \mathbf{p}'$  is the 3-momentum transfer, and  $B, R$  are relativistic correction factors [9]. For the color factors,  $\mathcal{F}^{C,S}$ , of the different two-body channels we use Casimir scaling for both Coulomb and string potentials, albeit with absolute values for the latter to maintain a strictly positive string tension [31].

The Hamiltonian is temperature dependent through the input bare masses and potentials. This implies a modification of the standard thermodynamic relations as discussed in the appendix of Ref. [10], since we not only need

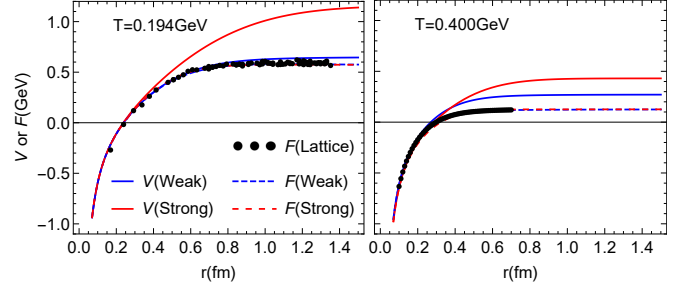


**Fig. 1.** The SCS (red) and WCS (blue) input potentials (solid lines) and resulting free energies (dashed lines), compared to IQCD free energies at temperatures of 194 MeV (left panel) and 400 MeV (right panel).

to consider the “evolution” of the states with temperature, but also the “evolution” of the operators. This is similar to the case of a time-dependent Hamiltonian, where the evolution of both operators and states figure. The fundamental Hamiltonian is time and temperature independent. The time or temperature dependent effective Hamiltonian represent a macroscopic average of microscopic processes, such as quark/gluon condensate physics (giving rise to effective masses) which is beyond the scope of our current work. To recover the original thermodynamics requires a more explicit treatment of the averaged microphysics in the masses and potentials, leading to an extra integral equation as suggested in the appendix in Ref. [10]. We defer these studies to future work.

The in-medium potential is constrained following Ref. [33] by calculating the static HQ free energy,  $F_{Q\bar{Q}}(r, T)$ , as well as quarkonium correlator ratios [8,9,26] within the  $T$ -matrix formalism. This includes imaginary parts in the 2-body potential and the single-quark propagators calculated selfconsistently from the heavy-light  $T$ -matrix. In this way, an ansatz for the input potential, taken to be of in-medium Cornell-type [34,35],

$$V_C + V_S = -\frac{4}{3} \alpha_s \frac{e^{-m_d r}}{r} - \frac{\sigma e^{-m_s r - (c_b m_s r)^2}}{m_s}, \quad (16)$$

is implemented into the  $T$ -matrix formalism, and its parameters ( $m_{d,s}$ ,  $\alpha_s$ ,  $\sigma$ ,  $c_b$ ) [10] are adjusted to IQCD data for  $F_{Q\bar{Q}}(r, T)$  [29] and pseudoscalar quarkonium correlators [36,37]. An extra term,  $-(c_b m_s r)^2$ , in the exponential of the string interaction is introduced to better capture the residual effects of string breaking in the QGP. The screening mass of the string term,  $m_s = (c_s m_d^2 \sigma / \alpha_s)^{1/4}$ , is obtained from a one-loop calculation for the Debye mass of  $V_S$  (cf. also Ref. [38]). The infinite distance limit of the color-singlet potential,  $-\frac{4}{3} \alpha_s m_d + \frac{\sigma}{m_s}$ , equals twice the Fock term for an individual static quark.

### 3 Inputs for Two Scenarios

The solution that can simultaneously fit the three sets of IQCD data ( $F_{Q\bar{Q}}$ , quarkonium correlators, EoS) is not

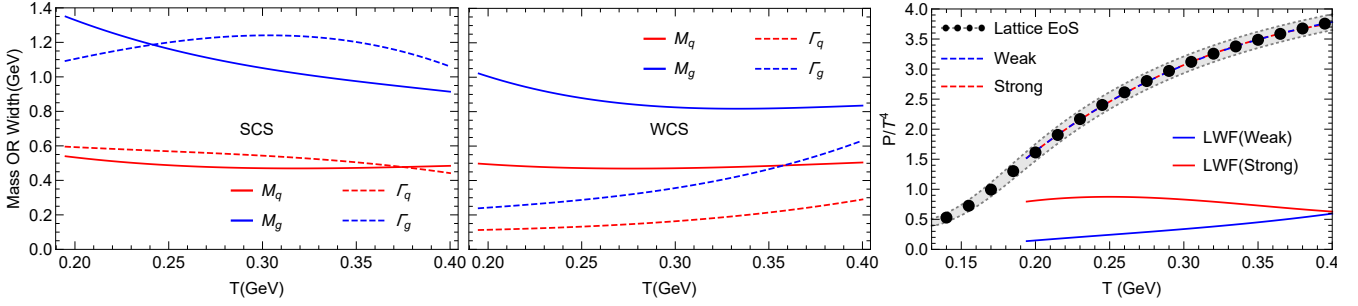


**Fig. 2.** Temperature dependence of the fitted masses (solid lines) and emerging widths (dotted lines) for quarks (red lines) and gluons (blue lines) for the SCS (left panel) and WCS (middle panel), as figuring in the description of the pressure,  $P/T^4$ , from lQCD [28] (right panel).

unique. In this section, we discuss two representative solutions in terms of the SCS, characterized by a rather strong potential (with long-range remnants of the confining force in the QGP), and the WCS with a much weaker one close to the free energy itself, cf. Fig. 1. The parameter values for the SCS figuring in Eq. (16) from the selfconsistent fits are:  $c_b=1.3$ ,  $\alpha_s=0.270$ ,  $\sigma=0.225 \text{ GeV}^2$ ,  $m_d=-0.238 \text{ GeV} + 2.915T$ , and  $c_s=0.01$ . Compared to previous work [9], the Casimir-scaled string term enables a better description of the color-octet free energy (not shown here). For the WCS we have:  $c_b=1.3$ ,  $\alpha_s=0.270$ ,  $\sigma=0.210 \text{ GeV}^2$ ,  $m_d=0.975 \text{ GeV}-0.135 \text{ GeV}^2/T$ , and  $c_s=0.1$ . These two quite simple parameterizations result in a rather good fit of the full numerical results to the lQCD data [10].

While the EoS is part of the overall nested fitting procedure, it involves more directly the bare-quark ( $M_q$ ) and -gluon ( $M_g$ ) masses in the Hamiltonian, which are added to the selfconsistent Fock-masses. They provide the main handle to reproduce the lQCD data for the QGP pressure [10]. This is done by numerical iteration to selfconsistently solve the  $T$ -matrices, Eq. (8), and selfenergies, Eq. (13), for a trial mass value, and evaluate the matrix-log for the LWF  $\Phi$  (including all two-body color and flavor channels [39] with spin degeneracy and angular momenta up to  $l=5$ , corresponding to 60 different  $T$ -matrices in the light sector [10].) At low temperatures,  $M_q/M_g$  approaches  $C_F/C_A=4/9$ , the ratio of Casimir factors for fundamental and adjoint representations in  $SU_C(3)$ , reflecting the infinite-distance limits of the static potential. At high temperature, the ratio  $M_q/M_g$  approaches the perturbative value,  $\sqrt{1/3}/\sqrt{3/4}$  [40]. This setup for the masses thus mimics a dynamical mass generation from confinement (via the 1-body selfenergy from the long-distance limit of the confining force), see Ref. [10] for further details.

The resulting “thermal” quark and gluon masses are comparable in magnitude to those extracted from quasiparticle model fits to the EoS [41, 40, 42, 43], although the temperature dependence found here is weaker, especially for the quark masses at temperatures approaching  $T_{pc}$  (from above), cf. the left and middle panels of Fig. 2. The gluon masses in the SCS are slightly larger than in the WCS, as they are selfconsistently related to the potentials as mentioned above [10]. While the parton masses

are comparable between the SCS and WCS, the deviations between their potentials are much more significant, which will lead to quite different predictions for the spectral and transport properties, as will be discussed in the following two sections.

## 4 Spectral Properties of Two Scenarios

In this section, we focus on the emerging spectral properties within the two solutions, first for the SCS in Sec. 4.1 and then for the WCS in Sec. 4.2.

### 4.1 SCS

The increasing role of the LWF, which encodes the bound-state contributions [44], as  $T_{pc}$  is approached from above suggests a transition from parton quasiparticles to hadronic degrees of freedom (see right panel of Fig. 2). This is a dynamical transition driven by an increasing interaction strength (due to a reduced screening in the potential) which is very different from quasiparticle models where parton degrees of freedom are suppressed kinematically by an increasing mass. Our interpretation is corroborated upon inspecting the selfconsistent spectral functions implicit in the calculation, plotted in Fig. 3 for partons and in Fig. 4 for their two-body interaction (imaginary part of  $T$  matrices). At low temperatures and 3-momenta, the light-quark spectral functions are strongly broadened with their strength spread over an energy range of about 1 GeV (cf. left panels in Fig. 3). This is well above their mass values, implying a loss of quark quasiparticles at small wavelengths in the QGP, again very different from quasiparticle-type models [40, 42, 43] where the quark widths are zero or small compared to their masses. In addition, large negative real parts of the low-energy selfenergy,  $\text{Re}\Sigma(\omega, p)$ , generate a low-energy solution for the dispersion relation,  $\omega - \sqrt{M^2 + p^2} - \text{Re}\Sigma(\omega, p) \sim 0$ , corresponding to a collective mode caused by off-shell interactions through near-threshold resonances in the  $T$ -matrix bound states which emerge at low temperature, cf. left panels in Fig. 4. The situation is similar for gluons (lower left panels of Fig. 3) and their interaction amplitudes (second panel in Fig. 4).



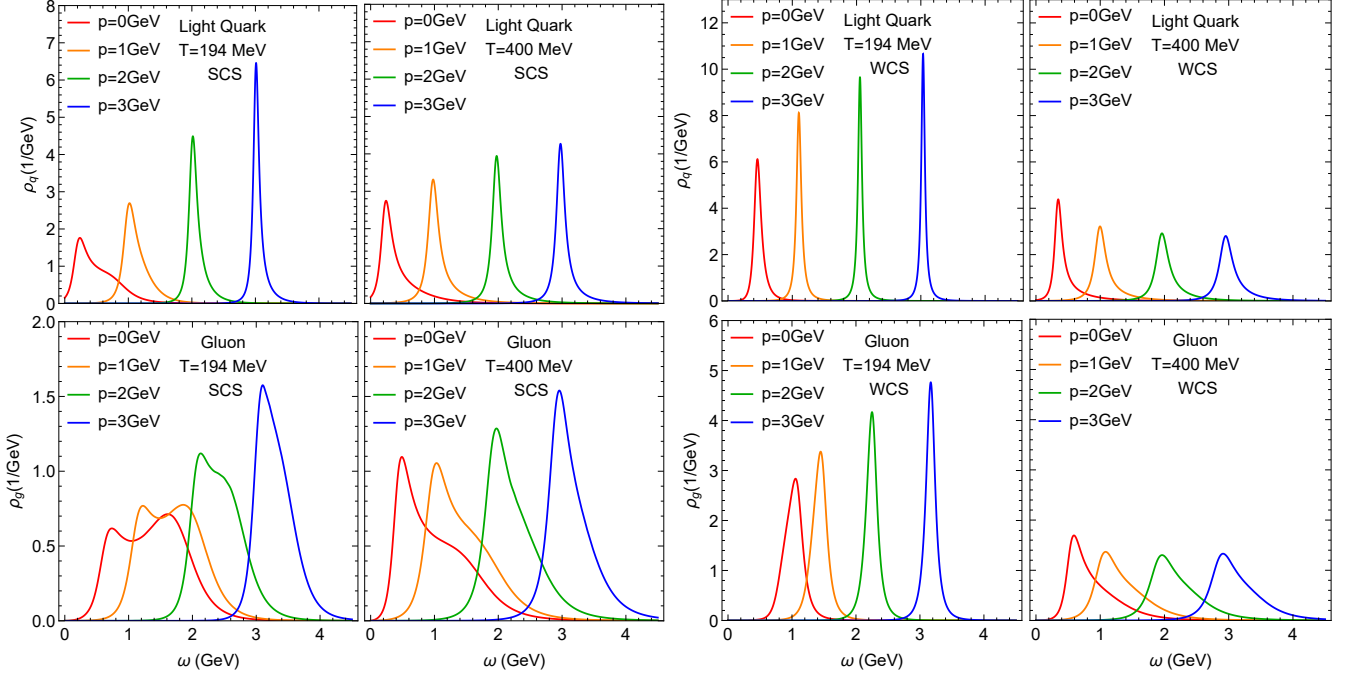


**Fig. 3.** In-medium spectral functions for quarks (upper panels) and gluons (lower panels) in the SCS (left panels, for  $T=194$  MeV and  $T=400$  MeV) and WCS (right panels, for  $T=194$  MeV and  $T=400$  MeV) for 3-momenta  $p=0,1,2,3$  GeV (color coding).

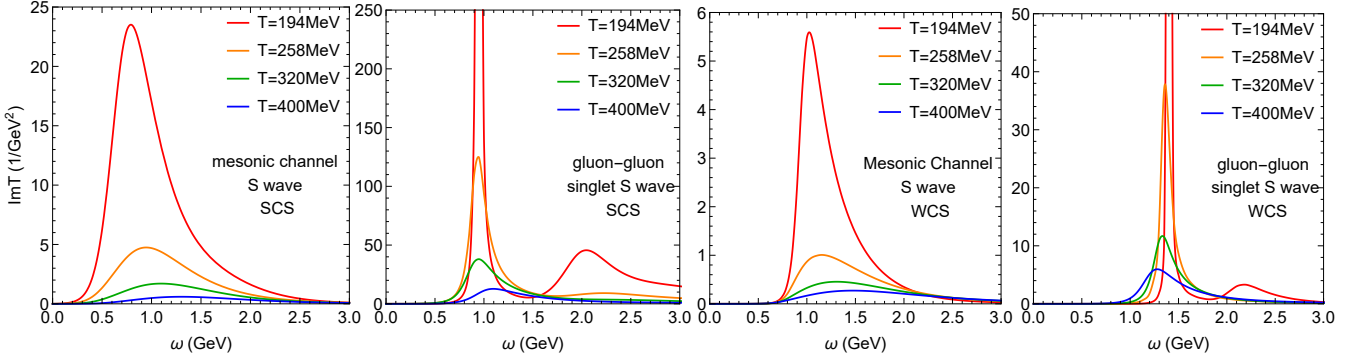


**Fig. 4.** Two examples of imaginary parts of two-body  $T$ -matrices (of a total of 60 included in the LWF), for the color-singlet  $S$ -wave  $q\bar{q}$  and  $gg$  channels for the SCS (left panels) and WCS (right panels) at different temperatures (color-coded).

Their spectral distributions also develop low-energy collective modes well below the nominal thermal gluon mass and 2-gluon threshold, respectively. However, the large mass of gluons near  $T_{pc}$  suggests that they largely decouple from the hadronization process of the system.

Despite the large increase in the degrees of freedom with temperature, the parton widths  $\Gamma_{q,g}$  vary little in the SCS, cf. left panel in Fig. 2. This is quite different from the perturbative expectation,  $\Gamma \propto g^2 T$ , and another manifestation of the increase in interaction strength as  $T \rightarrow T_{pc}$  from above. This increase is largely driven by the formation of pre-hadronic resonances as discussed above. With increasing temperature, the resonances dissolve, which, in turn, leads to better defined partonic quasiparticles. In this sense, our selfconsistent approach exhibits a smooth transition from hadronic to quark degrees of freedom as

temperature (or 3-momentum) increases. We also note that the color-singlet  $q\bar{q}$   $S$ -wave bound-state mass of  $\sim 0.8$  GeV near  $T_{pc}$  (left panel of Fig. 4) is intriguingly close to the vacuum  $\rho$ -meson mass, with a broad spectral function not unlike results from in-medium hadronic calculations [45]. Its large width suggests that the dissociation and regeneration rate of hadronic states is quite large, which may give a microscopic justification of why statistical hadronization is a good approximation for the dynamical hadronization within a transport approach.

#### 4.2 WCS

In the WCS, the interaction contribution to the total pressure represented by the LWF remains quite low even as the temperature approaches  $T_{pc}$ , cf. right panel of Fig. 2.

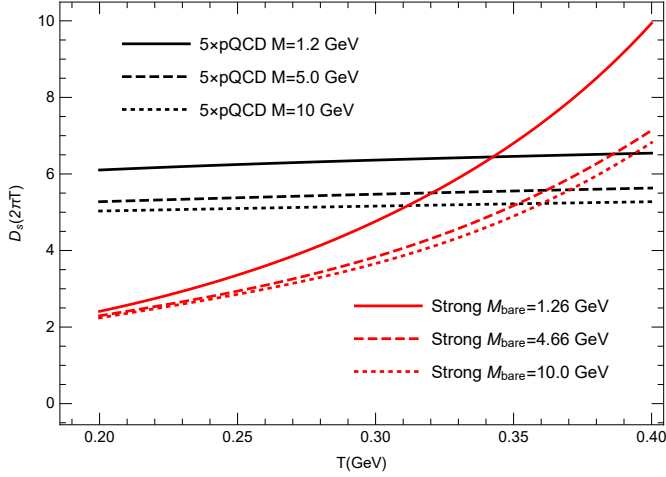


**Fig. 5.** Temperature dependence of the dimensionless HQ diffusion coefficient,  $\mathcal{D}_s(2\pi T)$ , for pQCD Born calculations (including an overall factor  $K$ -factor of 5 in the relaxation rate; black lines) and the SCS (red lines). The solid, dashed and dotted lines are for  $c$ ,  $b$  and  $b^+$  quarks, respectively. The in-medium mass  $\Delta M(T)$  of SCS is discussed in Ref [10]

This suggests that there is no transition in the degrees of freedom of the system, which is supported by the spectral functions of the light partons remaining quasiparticle-like down to low temperatures (cf. right panels in Fig. 3). Indeed, the pertinent widths,  $\Gamma_{q,g}$ , shown in middle panel of Fig. 2, stay well below their masses. Their increase with temperature is slightly faster than linear, presumably caused by the slower-than-linear increase of the screening masses figuring in the WCS potential.

The strength of two-body  $T$ -matrix amplitudes is much reduced in the WCS, by roughly a factor of 5 at the lowest temperature, cf. the two right panels in Fig. 4. The small amplitudes lead to small collision rates of the partons which is the reason for maintaining quasiparticle-like spectral functions at all temperatures and 3-momenta. The resonance peak of the  $S$ -wave mesonic channel is at around 1 GeV, just above the two-particle threshold. The latter feature is probably the main reason why the width of the threshold resonances at small temperature is not dramatically smaller than in the SCS.

## 5 Transport Properties of Two Scenarios

We now utilize our results to compute two prominent transport coefficients of the QGP, the spatial heavy-quark diffusion coefficient,  $\mathcal{D}_s$ , and the shear viscosity  $\eta$ . Since temperature is a macroscopic external parameter for time evolution in the linear response theory, and since the latter does not affect the temperature or other macroscopic properties of the background medium, the usual theoretical tools for evaluating transport coefficients, such as the Kubo formula, should still work for our temperature-dependent Hamiltonian.

For  $\mathcal{D}_s$ , we employ the formalism of Refs. [9, 26] with an additional off-shell extension [54] to account for the quantum effects of the HQ spectral functions as discussed in Ref. [55]. Schematically, the pertinent friction coefficient can be expressed as

$$A(p) = \left\langle \left(1 - \frac{\mathbf{p} \cdot \mathbf{p}'}{p^2}\right) \rho_i \rho_i \rho_Q \right\rangle \quad (17)$$

where  $\mathbf{p}(\mathbf{p}')$  is the incoming (outgoing) HQ quark momentum and the  $\rho_{i(Q)}$  are the light-parton (HQ) spectral functions. The diffusion coefficient follows from the zero-momentum limit of the friction coefficient,  $\mathcal{D}_s = T/(A(p=0)m_Q)$ , where  $m_Q$  denotes the HQ mass. In addition to its temperature dependence, the HQ mass dependence of  $\mathcal{D}_s$  is of considerable interest. A mass independence would be an important feature to consider  $\mathcal{D}_s$  as a universal coefficient of the medium. Indeed, the leading mass dependence is divided out in its relation to the HQ relaxation rate,  $A(p=0)$ , whose decrease with  $m_Q$  simply reflects the kinetic property that heavier quarks take longer to thermalize. We have therefore conducted calculations for charm quarks, bottom quarks and a still heavier quark (which we denote by  $b^+$ ) with about twice the  $b$ -quark mass. In Fig. 5 we plot our results for  $2\pi T \mathcal{D}_s$ , scaled dimensionless by the thermal wavelength of the medium  $1/2\pi T$ . Let us first inspect the results of time-honored perturbative QCD (pQCD) calculations using the leading-order Born diagrams for HQ scattering off thermal partons [56] (also including an overall  $K$  factor which is of no relevance in the present discussion). They are essentially constant with temperature and vary only weakly with  $m_Q$ , by up to 15%. The  $m_Q$  dependence suggests a saturation for large  $m_Q$ , thus converging toward a universal behavior (which is reasonably well realized already by  $b$  quarks). In the SCS, we observe a rather pronounced temperature dependence reflecting the reduced interaction strength in the QGP as  $T$  increases. However, the  $m_Q$  dependence also exhibits non-trivial behavior, with a near degeneracy at low  $T$  which is lifted as  $T$  increases. The spread in  $m_Q$  remains small for  $b$  and  $b^+$  quarks even at higher  $T$ , indicating a good universality in  $m_Q$ , while the latter is broken for  $c$  quarks indicating that  $m_c/T$  is becoming too small. The genuine (universal) temperature dependence in the HQ interaction strength is thus represented by the  $b$  and  $b^+$  quark curves. This reiterates the importance of high-precision bottom transport observables in URHICs.

For  $\eta$ , we employ the standard Kubo formula using the leading-density energy-momentum tensor [57] with relativistic extension,

$$\eta = \lim_{\omega \rightarrow 0} \sum_i \frac{\pi d_i}{\omega} \int \frac{d^3 \mathbf{p} d\lambda}{(2\pi)^3} \frac{p_x^2 p_y^2}{\varepsilon_i^2(p)} \rho_i(\omega + \lambda, p) \rho_i(\lambda, p) \times [n_i(\lambda) - n_i(\omega + \lambda)], \quad (18)$$

where the  $n_i(\omega)$  are the thermal distribution functions of light partons and  $d_i$  the pertinent degeneracies. Higher-order corrections are expected to be small [58, 59, 60, 61, 62]. For example, in Refs. [61, 63] second-order contributions have been found with a parametric dependence of

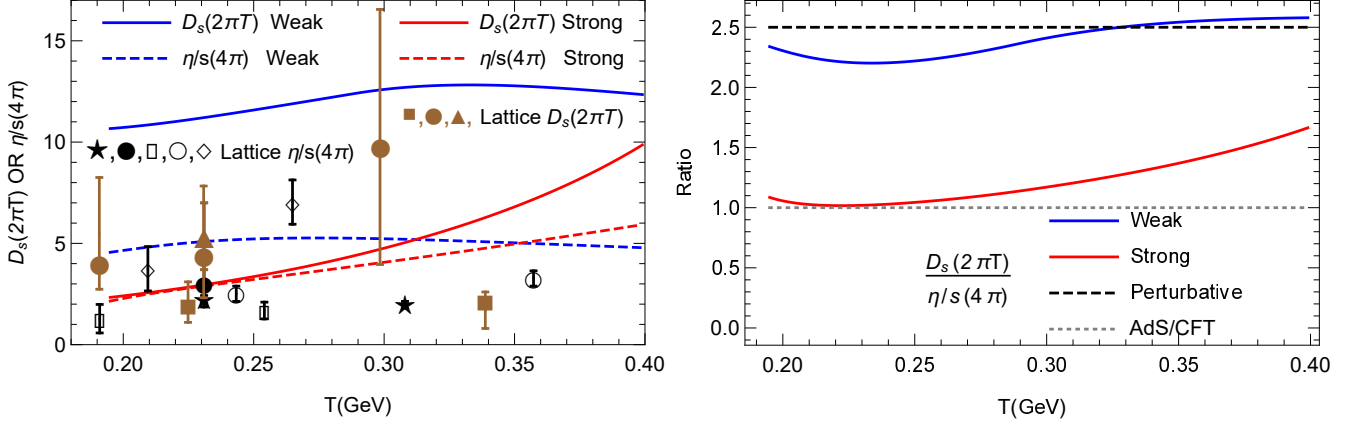


**Fig. 6.** Left panel: Specific viscosity,  $4\pi\eta/s$  (dashed lines), and charm-quark diffusion coefficient scaled by the thermal wavelength,  $D_s(2\pi T)$  (solid lines) for the SCS (red lines) and WCS (blue lines), compared to IQCD data ( $\{\star$  [46],  $\bullet$  [47],  $\square$  [48],  $\circ$  [49],  $\diamond$  [50]] for  $4\pi\eta/s$  in black and  $\{\blacksquare$  [51],  $\bullet$  [52],  $\blacktriangle$  [53]] for  $D_s(2\pi T)$  in brown). Right panel: the ratio  $[(2\pi T)D_s]/[4\pi\eta/s]$  for SCS (red solid line) and WCS (blue solid line) compared to perturbative (dashed line) and AdS/CFT (dotted line) limits.

$1/\Gamma^2$  (with  $1/\Gamma$  for the leading loop). This suggests that for strongly coupled systems, with large particle widths, higher-order contributions are suppressed. A more systematic study to include higher-order corrections to the viscosity as discussed in Ref. [63] will be reported elsewhere.

Before discussing the numerical results of the SCS and WCS, let us recall two limiting cases [64] which will be instructive for comparisons with our results. In the strongly coupled limit, AdS/CFT approaches have been used to calculate the transport coefficients of interest here. The spatial HQ diffusion coefficient was found at  $D_s \approx 1/(2\pi T)$  [66, 67]. Also, the shear viscosity is conjectured to reach a universal strongly-coupled limit of  $\eta/s = 1/(4\pi)$  [68, 69], where  $s$  denotes the entropy density. This suggests a relation

$$(2\pi T D_s) \approx 1 \times (4\pi\eta/s) \quad (19)$$

in a strongly-coupled system. For a weakly-coupled massless gas, the viscosity can be evaluated in a classical kinetic theory as [70]

$$\eta/s \approx \left(\frac{4}{15} n\langle p \rangle \lambda_{tr}\right)/s = \frac{1}{5} T \lambda_{tr} \quad (20)$$

with  $n\langle p \rangle = \varepsilon$  and  $Ts = \varepsilon + P = 4/3\varepsilon$ . Here,  $n$ ,  $\varepsilon$  and  $P$  denote the particle density, energy density and pressure, respectively. Using a momentum transfer mean-free-path of  $\lambda_{tr} \approx \tau_{tr} \approx \tau_Q m_Q/T = D_s$  where  $\tau_{tr}$  and  $\tau_Q$  are mean-free-time and HQ relaxation time, we obtain a relation

$$(2\pi T D_s) \approx 5/2 \times (4\pi\eta/s) \quad (21)$$

for a weakly-coupled system.

In the left panel of Fig. 6 we plot the dimensionless-scaled transport coefficients together with the pertinent IQCD data. The hierarchy between SCS and WCS basically reflects the interaction strength of the two scenarios, with the former leading to smaller values due to larger scattering rates. For the SCS at low temperatures, both

coefficients are at approximately twice the value for the conjectured lower quantum bounds. It is interesting to note that the relatively close proximity to the quantum bounds is accompanied by the loss of (long-wavelength) quasiparticles in the system [68, 63], as discussed in the previous section. For the WCS, the low-temperature  $c$ -quark diffusion coefficient is about a factor of 5 larger than in the SCS, but only about a factor  $\sim 2$  for the viscosity. Overall, the IQCD data favor the SCS. In the SCS, there is a clear trend for the coefficients to increase with temperature, toward a more weakly-coupled medium. However, from inspecting the individual coefficients alone, it is not easy to tell what really constitutes the notion of a weakly- or strongly-coupled medium.

We therefore propose the ratio  $[(2\pi T)D_s]/[4\pi\eta/s]$  as a quantity to better distinguish strongly- and weakly-coupled media, cf. the right panel of Fig. 6. As argued with Eq. (21) and Eq. (19), this ratio is expected to be 1 in the strongly- and 5/2 in the weakly-coupled limit. Interestingly, this ratio is indeed close to one in the SCS at low temperature, increasing toward higher temperatures, yet still significantly below 5/2 even at  $T=400$  MeV (where hydrodynamics is still believed to work well in URHICs); we recall, however, that (part of) this increase is presumably due to the relatively small  $c$ -quark mass; it is less in the HQ limit. On the other hand, the ratio in the WCS is close to 5/2 even at low temperature (despite the rather small specific viscosity), with insignificant temperature dependence.

## 6 Conclusions

In the present work we have utilized our earlier developed nonperturbative quantum many-body approach to the QGP to analyze its transport properties. First, we have rederived in full 4D the selfconsistent all-order resummed Luttinger-Ward functional, which plays a key role in the description of QGP structure especially at low temperatures, where it accounts for dynamically formed

bound states as a mechanism for a gradual transition from partonic to hadronic degrees of freedom. After briefly reviewing the essential features of two solutions in fits to lQCD data for HQ and bulk properties (EoS), corresponding to a “strong” and “weak” underlying potential scenario (SCS and WCS), we have calculated pertinent transport coefficients, in particular the specific shear viscosity and the HQ diffusion coefficient. For the latter, we have investigated its dependence on the HQ mass and found that for bottom quarks it is close to a universal limit for large  $m_Q$ , while for charm quarks it can be significantly larger, especially toward higher temperatures. In the SCS, it turns out that both the specific shear viscosity and the scaled HQ diffusion coefficient are at about 2 times their conjectured lower quantum bound at temperatures near  $T_{pc}$ , and gradually increasing with temperature. The results of the SCS are in a favorable range for URHIC phenomenology using hydrodynamic bulk evolution models for light hadron spectra and HF transport approaches for HF observables. On the other hand, in the WCS, the transport parameters are markedly larger, in a range which is incompatible with experimental observations. Thus, the transport coefficients, when put into context with URHIC phenomenology, can discriminate the SCS and WCS solutions, which was not possible on the basis of the fits to lQCD data alone. We have then proposed the ratio of the HQ diffusion coefficient over specific viscosity as a more quantitative measure of the notion of a weakly vs. a strongly coupled medium, with limiting values of  $5/2$  vs.  $1$ , respectively. Somewhat surprisingly, the results for the WCS turn out to be close to the former over the considered temperature range, while the SCS results are close to one near  $T_{pc}$ . Recalling the underlying spectral properties of the two scenarios, with the melting of parton quasiparticle structures in the SCS at large wavelength and low  $T$ , while quasiparticles prevail in the WCS at all  $p$  and  $T$ , we corroborate earlier qualitative expectations along these lines. We also recall that the key agent in the strong coupling properties are long-range remnants of the confining force (which are prominent in the SCS but not in the WCS potential), thus suggesting an intimate connection between confinement and the strongly coupled QGP.

## Acknowledgements

This work has been supported by the U.S. NSF through grant nos. PHY-1614484 and PHY-1913286.

## References

1. C. Ratti, Rept. Prog. Phys. 81 (2018) 084301.
2. S.x. Qin and D.H. Rischke, Phys. Rev. D 88 (2013) 056007.
3. C.S. Fischer et al., Phys. Rev. D 98 (2018) 014009.
4. N. Khan et al., (2015), arXiv:1512.03673.
5. T.K. Herbst et al., Phys. Lett. B 731 (2014) 248.
6. K. Fukushima and V. Skokov, Prog. Part. Nucl. Phys. 96 (2017) 154.
7. N.U.F. Bastian and D.B. Blaschke, (2018), 1812.11766.
8. D. Cabrera and R. Rapp, Phys. Rev. D 76 (2007) 114506.
9. F. Riek and R. Rapp, Phys. Rev. C 82 (2010) 035201.
10. S.Y.F. Liu and R. Rapp, Phys. Rev. C 97 (2018) 034918.
11. U. Heinz and R. Snellings, Ann. Rev. Nucl. Part. Sci. 63 (2013) 123, 1301.2826.
12. J.E. Bernhard et al., Phys. Rev. C 94 (2016) 024907.
13. H. Niemi, K.J. Eskola and R. Paatelainen, Phys. Rev. C 93 (2016) 024907.
14. R. Rapp et al., Nucl. Phys. A 979 (2018) 21.
15. S. Cao et al., Phys. Rev. C 99 (2019) 054907.
16. J.M. Luttinger and J.C. Ward, Phys. Rev. 118 (1960) 1417.
17. G. Baym and L.P. Kadanoff, Phys. Rev. 124 (1961) 287.
18. G. Baym, Phys. Rev. 127 (1962) 1391.
19. S.Y.F. Liu and R. Rapp, J. Phys. Conf. Ser. 779 (2017) 012034.
20. J.P. Blaizot, E. Iancu and A. Rebhan, Phys. Rev. D 63 (2001) 065003.
21. M.I. Haftel and F. Tabakin, Nucl. Phys. A 158 (1970) 1.
22. J.P. Blaizot and G. Ripka, Quantum theory of finite systems (MIT press Cambridge, 1986).
23. R. Haussmann et al., Phys. Rev. A 75 (2007) 023610.
24. R.M. Woloshyn and A.D. Jackson, Nucl. Phys. B 64 (1973) 269.
25. M. Mannarelli and R. Rapp, Phys. Rev. C 72 (2005) 064905.
26. F. Riek and R. Rapp, New J. Phys. 13 (2011) 045007.
27. S. Borsanyi et al., JHEP 11 (2010) 077.
28. HotQCD Collaboration, A. Bazavov et al., Phys. Rev. D 90 (2014) 094503.
29. A. Mocsy, P. Petreczky and M. Strickland, Int. J. Mod. Phys. A 28 (2013) 1340012.
30. O. Kaczmarek, PoS CPOD07 (2007) 043.
31. P. Petreczky and K. Petrov, Phys. Rev. D 70 (2004) 054503.
32. A. Bazavov, Y. Burnier and P. Petreczky, Nucl. Phys. A 932 (2014) 117.
33. S.Y.F. Liu and R. Rapp, Nucl. Phys. A 941 (2015) 179.
34. E. Megias, E. Ruiz Arriola and L. Salcedo, JHEP 0601 (2006) 073.
35. E. Megias, E. Ruiz Arriola and L. Salcedo, Phys. Rev. D 75 (2007) 105019.
36. G. Aarts et al., Phys. Rev. D 76 (2007) 094513.
37. G. Aarts et al., JHEP 11 (2011) 103.
38. Y. Burnier, O. Kaczmarek and A. Rothkopf, JHEP 12 (2015) 101.
39. E.V. Shuryak and I. Zahed, Phys. Rev. D 70 (2004) 054507.
40. P. Levai and U.W. Heinz, Phys. Rev. C 57 (1998) 1879.
41. A. Peshier and W. Cassing, Phys. Rev. Lett. 94 (2005) 172301.
42. S. Plumari et al., Phys. Rev. D 84 (2011) 094004.
43. H. Berrehrah et al., Int. J. Mod. Phys. E 25 (2016) 1642003.
44. R. Rapp and J. Wambach, Phys. Lett. B 315 (1993) 220.
45. R. Rapp, J. Wambach and H. van Hees, Landolt-Bornstein 23 (2010) 134.
46. S. Borsanyi et al., Phys. Rev. D 98 (2018) 014512.
47. S.W. Mages et al., PoS LATTICE2014 (2015) 232.
48. H.B. Meyer, Phys. Rev. D 76 (2007) 101701.
49. H.B. Meyer, Nucl. Phys. A 830 (2009) 641C.
50. A. Nakamura and S. Sakai, Phys. Rev. Lett. 94 (2005) 072305.
51. H.T. Ding et al., Phys. Rev. D 86 (2012) 014509.



- 52. D. Banerjee et al., Phys. Rev. D 85 (2012) 014510.
- 53. A. Francis et al., Phys. Rev. D 92 (2015) 116003.
- 54. P. Danielewicz, Annals Phys. 152 (1984) 239.
- 55. S.Y.F. Liu, M. He and R. Rapp, Phys. Rev. C 99 (2019) 055201.
- 56. B. Svetitsky, Phys. Rev. D 37 (1988) 2484.
- 57. D.N. Zubarev, Nonequilibrium statistical thermodynamics (Plenum Publishing Corporation, 1974).
- 58. M. Iwasaki, H. Ohnishi and T. Fukutome, (2006), hep-ph/0606192.
- 59. M. Iwasaki, H. Ohnishi and T. Fukutome, J. Phys. G 35 (2008) 035003.
- 60. R. Lang and W. Weise, Eur. Phys. J. A 50 (2014) 63.
- 61. S. Ghosh, Int. J. Mod. Phys. A 29 (2014) 1450054.
- 62. N. Christiansen et al., Phys. Rev. Lett. 115 (2015) 112002.
- 63. T. Enss, R. Haussmann and W. Zwerger, Annals Phys. 326 (2011) 770.
- 64. R. Rapp and H. van Hees, Quark-Gluon Plasma 4, edited by R. Hwa and X.N. Wang, p. 111, World Scientific, Singapore, 2010, arXiv:0903.1096.
- 65. S.S. Gubser, Phys. Rev. D 74 (2006) 126005.
- 66. J. Casalderrey-Solana and D. Teaney, Phys. Rev. D 74 (2006) 085012.
- 67. S.S. Gubser, Phys. Rev. D 76 (2007) 126003.
- 68. P. Kovtun, D.T. Son and A.O. Starinets, Phys. Rev. Lett. 94 (2005) 111601.
- 69. A. Buchel, J.T. Liu and A.O. Starinets, Nucl. Phys. B 707 (2005) 56.
- 70. P. Danielewicz and M. Gyulassy, Phys. Rev. D 31 (1985) 53.